

Effects of Cavern Depth on Surface Subsidence and Storage Loss of Oil-Filled Caverns

Edward L. Hoffman
Engineering and Structural Mechanics Division
Sandia National Laboratories
Albuquerque, New Mexico 87 185

Abstract

Finite element analyses of oil-filled caverns were performed to investigate the effects of cavern depth on surface subsidence and storage loss, a primary performance criteria of SPR caverns. The finite element model used for this study was axisymmetric, approximating an infinite array of caverns spaced at 750 ft. The stratigraphy and cavern size were held constant while the cavern depth was varied between 1500 ft and 3000 ft in 500 ft increments. Thirty year simulations, the design life of the typical SPR cavern, were performed with boundary conditions modeling the oil pressure head applied to the cavern lining. A depth dependent temperature gradient of 0.012" F/ft was also applied to the model. The calculations were performed using ABAQUS, a general purpose finite element analysis code. The user-defined subroutine option in ABAQUS was used to enter an elastic secondary creep model which includes temperature dependence.

The calculations demonstrated that surface subsidence and storage loss rates increase with increasing depth. At lower depths the difference between the lithostatic stress and the oil pressure is greater. Thus, the effective stresses are greater, resulting in higher creep rates. Furthermore, at greater depths the cavern temperatures are higher which also produce higher creep rates. Together, these factors result in faster closure of the cavern. At the end of the 30 year simulations, a 1500 ft-deep cavern exhibited 4 percent storage loss and 4 ft of subsidence while a 3000 ft-deep cavern exhibited 33 percent storage loss and 44 ft of subsidence. The calculations also demonstrated that surface subsidence is directly related to the amount of storage loss. Deeper caverns exhibit more subsidence because the caverns exhibit more storage loss. However, for a given amount of storage loss, nearly the same magnitude of surface subsidence was exhibited, independent of cavern depth.

Contents

Figures	6
Tables..	7
1 INTRODUCTION	9
2 FINITE ELEMENT MODELS	9
2.1 Cavern Geometry	9
2.2 Problem Parametrization	9
2.3 Structural Model	9
2.4 Thermal Model	13
2.5 Constitutive Models and Material Properties	13
3 ANALYSIS RESULTS	15
3.1 Storage Loss	16
3.2 Surface Subsidence	17
3.3 Comparison of Analysis Results to Field Measurements	25
4 CONCLUSIONS	28
5 REFERENCES	29
Distribution	30

Figures

1	Stratigraphy used in variable depth calculations (not to scale).	10
2	Finite element models of SPR cavern at depths of 1500, 2000, 2500 and 3000 ft (boundary conditions shown on 1500 ft-deep model only).	11
3	Well pressure calculated based on depth of cavern floor and difference between brine and second fluid (freshwater or oil) densities.	12
4	Surface subsidence as a function of time for the 3000 ft-deep cavern.	15
5	Deformed cavern shape of the 3000 ft-deep cavern at $t=30$ years.	16
6	Accumulated storage loss distribution for the 3000 ft-deep cavern as a function of distance measured from the cavern floor to the ceiling. The accumulated storage loss is normalized with respect to total storage loss.	17
7	Cavern volume, storage loss and subsidence volume as a function of time for a 1500 ft-deep cavern.	18
8	Cavern volume, storage loss and subsidence volume as a function of time for a 2000 ft-deep cavern.	18
9	Cavern volume, storage loss and subsidence volume as a function of time for a 2500 ft-deep cavern.	19
10	Cavern volume, storage loss and subsidence volume as a function of time for a 3000 ft-deep cavern.	19
11	Percent storage loss as a function of time for cavern depths of 1500, 2000, 2500, and 3000 ft.	20
12	Percent storage loss at 30 years as a function of cavern depth.	20
13	Storage loss rate as a function of time for cavern depths of 1500, 2000, 2500, and 3000 ft.	21
14	Surface subsidence as a function of time.	21
15	Surface subsidence at $t=30$ years as a function of cavern depth.	22
16	Subsidence rate as a function of time for cavern depths of 1500, 2000, 2500, and 3000 ft.	23
17	Fraction of storage loss converted to subsidence as a function of time.	23
18	Surface subsidence as a function of storage loss. Both variables are normalized with respect to the original cavern volume.	24
19	Difference between storage loss and subsidence volume for cavern depths of 1500, 2000, 2500, and 3000 ft.	25
20	Pressurization rate for the 2500 ft-deep cavern.	27

Tables

1	Structural Properties of Salt, Caprock , and Overburden	14
2	Measured Subsidence at West Hackberry Cavern 115	26
3	Measured Pressurization Data for West Hackberry Cavern 115	27

1 INTRODUCTION

Currently a typical Strategic Petroleum Reserve (SPR) cavern has a depth, measured from the top of the cavern to the surface, of 2500 ft and a cavern spacing of 750 ft. However, due to the possibility of expansion, there has been interest in evaluating caverns at other depths. Finite element analyses of oil-filled caverns were performed to investigate the effects of cavern depth on surface subsidence and storage loss.

The finite element model used for this study is axisymmetric, approximating an infinite array of caverns spaced at 750 ft. The stratigraphy and cavern size were held constant while the cavern depth was varied between 1500 ft and 3000 ft in 500 ft increments. The calculations were performed using ABAQUS, a general purpose finite element analysis code [1]. Input files for the finite element model were parameterized to simplify geometry changes. The finite element calculations consisted of two separate models: a structural model and a steady state thermal model. Only one-way thermal coupling was considered by entering the thermal results into the structural analyses. The user-defined subroutine option in ABAQUS was used to enter an elastic secondary creep model which includes temperature dependence.

In the following section, the finite element models and analysis procedures are described in detail. In Section Figure 3 the analysis results are presented. Finally, in Section Figure 4 the conclusions of the study are discussed.

2 FINITE ELEMENT MODELS

2.1 Cavern Geometry

The finite element models used for this study include a typical SPR stratigraphy of salt, caprock and overburden as illustrated in Figure 1. The overburden and caprock were assumed to be 1000 ft and 400 ft-thick, respectively. The cavern geometry chosen for the study is a 2000 ft-high right circular cylinder with a 200 ft diameter. This simplified geometry was chosen because it yields an oil storage capacity of $6.28 \times 10^7 \text{ ft}^3$ or 11.2 MMbbl, the volume of a typical SPR cavern.

2.2 Problem Parametrization

The input file for mesh generation was parameterized using *Aprepro* [2] in order to automate parametric changes. Using this code, all physical dimensions and material properties are entered as model parameters. Thus, when the cavern depth is changed, the boundary conditions applied to the cavern lining (well pressure, oil pressure, etc.) are recalculated. The use of this system has made model generation efficient for this study and will facilitate future parametric studies.

2.3 Structural Model

The four models shown in Figure 2 were generated with cavern depths of 1500, 2000, 2500, and 3000 ft. The cavern depth variations resulted in 100, 600, 1100, and 1600 ft of salt above the cavern roof. The thickness of the caprock (400 ft) and overburden (1000 ft) were unchanged. The boundary conditions applied to all four models are illustrated on the 1500 ft-deep cavern. The axis of symmetry is on the left side while the far field boundary is on the right. The far field boundary is 375 ft from the axis of symmetry. The distance between the

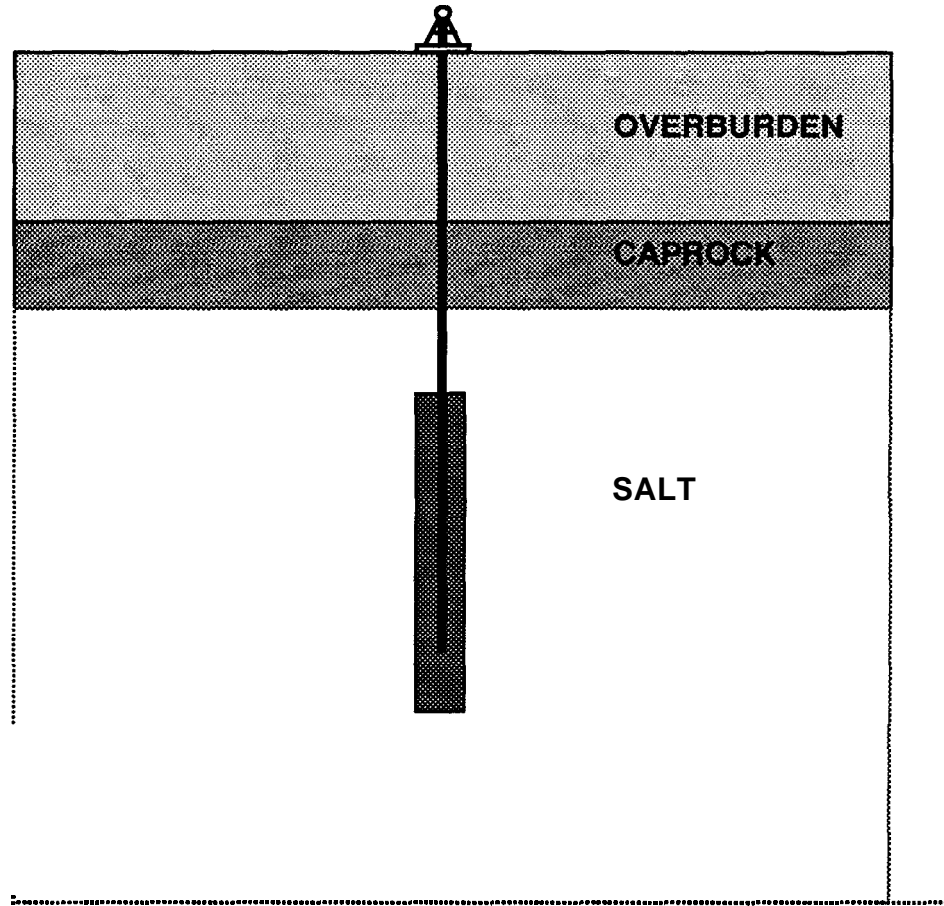


Figure 1. Stratigraphy used in variable depth calculations (not to scale).

bottom of the cavern and the lower boundary was held constant at 3280 ft for all four cases. Displacements at the far field and axis of symmetry were constrained in the radial direction. The lower boundary is constrained in the vertical direction. These boundary conditions approximate an infinite array of caverns, equally spaced at 750 ft, the typical spacing for SPR caverns. In an infinite array of equally spaced caverns, the planes of symmetry actually form polygons around each of the caverns. For the present study, the polygons were approximated as circles, resulting in an axisymmetric geometry. Load symmetry was also assumed, implying that all caverns in the array were constructed at the same time and experienced identical pressure histories.

The analyses presented in this memo were performed using ABAQUS, a general purpose finite element analysis code. Four-node, isoparametric, quadrilateral elements were used with reduced integration and hourglass control [1]. The first mesh illustrated in Figure 1 consists of 932 nodes and 860 elements, the second consists of 1016 nodes and 940 elements, the third consists of 1100 nodes and 1020 elements, and the fourth consists of 1184 nodes and 1100 elements. The number of elements in each model varies because the mesh refinement was

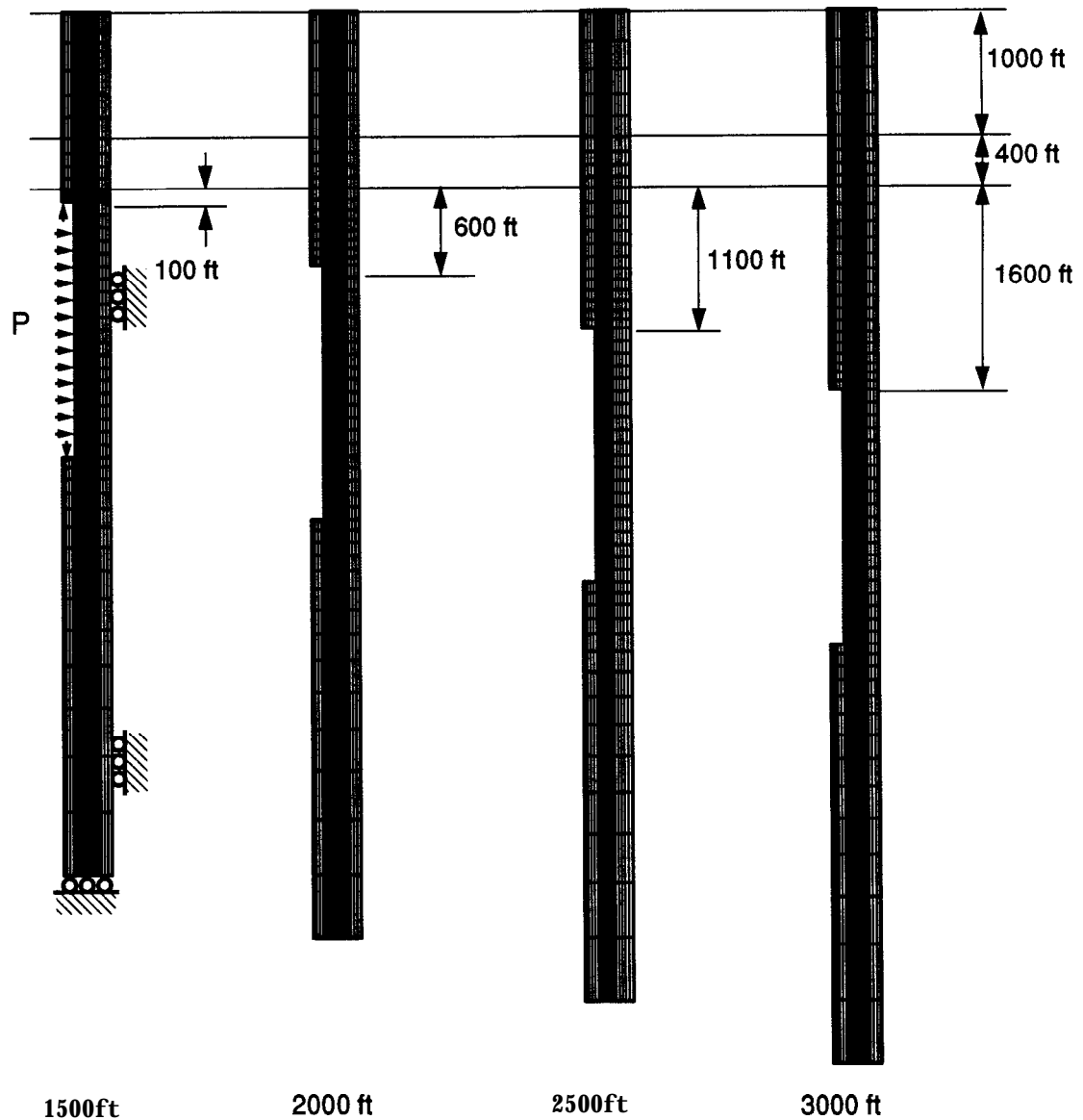


Figure 2. Finite element models of SPR cavern at depths of 1500, 2000, 2500 and 3000 ft (boundary conditions shown on 1500 ft-deep model only).

adjusted to account for the varying salt thickness above the cavern.

A pressure history is applied to the inside of the cavern during the first year of the analysis to simulate cavern formation. The simulation of cavern formation is approximated by a transition between two boundary conditions: one at $t=0$ and another at $t=1$ year. At time $t=0$, the pressure inside the cavern is equal to the lithostatic stress field of the salt. In this state, the effective stress field around the cavern is zero, resulting in no creep. At time $t=1$ year, the pressure applied to the inside of the cavern is equal to the hydrostatic pressure of freshwater. The freshwater head is used because, in the leaching phase, fresh water is pumped into the

cavern and brine flows out. In addition to the freshwater head, a uniform well pressure is applied to the lining of the cavern. The well pressure is based on the difference between brine gradient (0.52 **psi/ft**) and fresh water gradient (0.43 **psi/ft**) and the depth to the **freshwater-brine** interface as shown in Figure 3. The combination of these pressures simulates the pressure applied to the cavern lining during the leaching process. To transition smoothly between the two boundary conditions a weighting function (w) is defined as follows:

$$w = \frac{1 - t}{1} \quad \text{for } 0.0 \leq t \leq 1.0 \text{ year} \quad (1)$$

The lithostatic pressure is multiplied by w and the leaching pressure by $(1-w)$ so that the pressure applied to the lining of the cavern transitions linearly over the first year. This approximation circumvents the high creep strain rates resulting from instantaneous cavern formation.

After the first year, the oil pressure head is applied to the lining of the cavern and is maintained constant over the 30 year life of the cavern. The weight of the oil (0.37 **psi/ft**) resulted in a pressure gradient along the cavern lining with respect to elevation. In addition, a uniform well pressure, calculated as shown in Figure 3 (using oil as the second fluid) was added to the distributed pressure. The method used to calculate the uniform well pressure assumes a zero

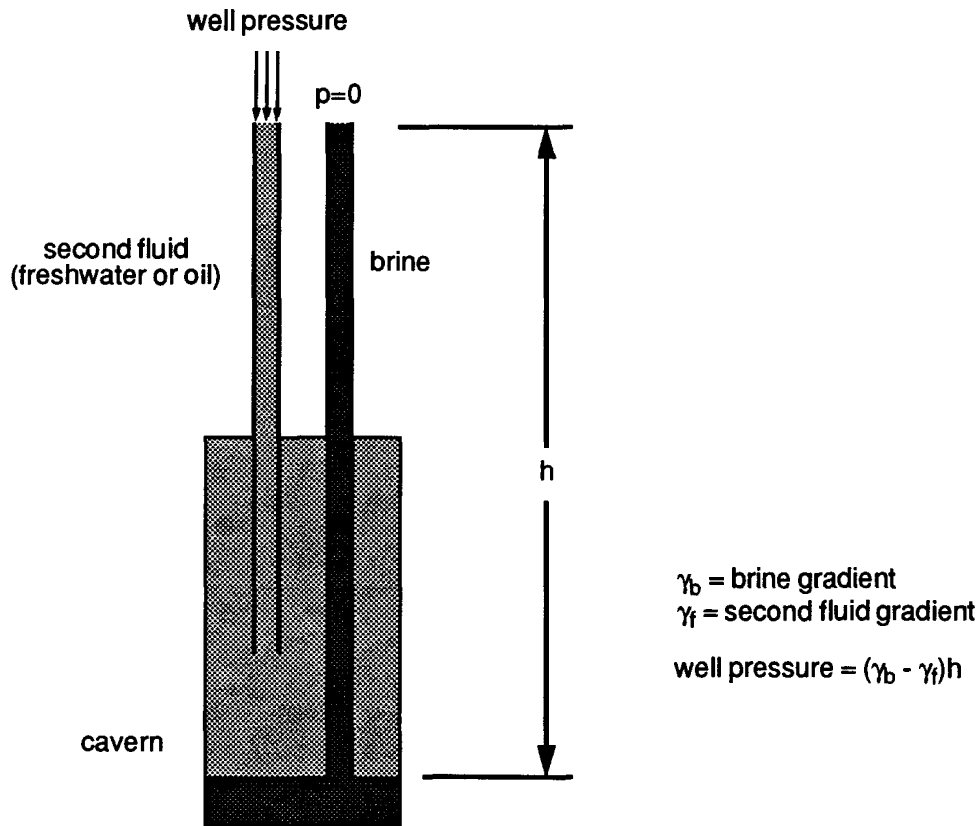


Figure 3. Well pressure calculated based on depth of cavern floor and difference between brine and second fluid (freshwater or oil) densities.

brine side pressure throughout the service life of the cavern.

In addition to the pressure loads, gravitational body forces are applied to the rock. **Elevation-**dependent initial stresses were applied so that the model is at equilibrium at time zero. In the elastic materials, the vertical stress component at a given location was applied based on the weight of the material above that point. The horizontal component was applied to be consistent with a vertically loaded elastic material in equilibrium. Under these load conditions, the resulting ratio of horizontal to vertical stress components is defined as follows:

$$\frac{\sigma_h}{\sigma_v} = \frac{\nu}{1-\nu} \quad (2)$$

where ν is the Poisson's ratio of the material. For the salt, an initial stress state was assumed in which the vertical and horizontal stress components are equal (lithostatic) to the weight of the overbearing material.

2.4 Thermal Model

The finite element model included a depth-dependent temperature gradient which started at 80° F at the surface and increased at the rate of 0.012° F/ft. The temperature distribution is important because the creep response of the salt is temperature dependent. Radial temperature gradients due to cooling effects of the oil were not considered in these calculations. The temperature field was calculated using the heat transfer solution module of ABAQUS and a linear four node quadrilateral element. A steady state analysis was run to develop the linear temperature gradient. In the analysis, appropriate temperatures were specified at the upper and lower boundaries. The thermal conductivities of all three materials were set equal in order to obtain a linear temperature field. The magnitude of the thermal conductivity is not reported since it was not critical to obtain a linear temperature field. Only one-way thermal coupling was considered by including the depth-dependent temperatures in the structural analysis. The thermal model used the same mesh as the structural model; thus, no interpolation was necessary to map the temperatures to the structural mesh. Using this procedure, temperatures were input into the structural analysis at the nodes and interpolated to the material points. The assumption of one-way coupling was appropriate since the deformations were not large enough to affect the thermal analysis.

2.5 Constitutive Models and Material Properties

The overburden and **caprock** were modeled as elastic materials using the properties listed in Table 1. The properties were obtained from [3] and were for homogeneous samples. The elastic properties for shale were used for the **caprock** and those of sandstone were used for the overburden. No approximation was made to account for **fracturing** of the overburden and **caprock** layers.

The domal salt exhibits both elastic and creep behavior. The constitutive model used for this material considered only secondary creep. The creep strain rate is determined from the effective stress as follows:

$$\dot{\epsilon}^{cr} = A \tilde{\sigma}^n \exp \left(-\frac{Q}{RT} \right) \quad (3)$$

where

$\dot{\epsilon}^{cr}$ is the creep strain rate,

$\tilde{\sigma}$ is the effective or von Mises stress,

T is absolute temperature,

A and n are constants determined from fitting the model to creep data,

Q is the effective activation energy (Cal/mole),

R is the universal gas constant (1545 ft·lb/(lb·mol)(°R)).

The secondary creep law contained in ABAQUS does not include the temperature dependence in Equation 3. Thus, the ABAQUS user subroutine capability was used to implement the creep law defined above. The creep constants for salt are given in Table 1 and correspond to parameters for the Waste Isolation Pilot Plant (WIPP) salt [4]. Previous studies have shown

Table 1: Structural Properties of Salt, Caprock, and Overburden

	Elastic Properties			Creep Properties		
Material	Young's Modulus, E (kpsi)	Poisson's Ratio, ν	Density, ρ (lb/in ³)	A (psi ^{-4.9} /sec)	n	Activation Energy, Q (ft·lb/mole)
Salt	3.60×10^5	0.25	0.083 1	3.73×10^{-17}	4.9	3.70×10^4
Caprock	1.02×10^6	0.29	0.0903	--	--	--
Overburden	1.45×10^4	0.33	0.0677	--	--	--

that WIPP and most SPR salts exhibit similar creep behavior [5, 6]. The Young's modulus for rock salt was reduced by a factor of 12.5 from its laboratory or reference value. This reduction has produced good agreement between predicted and measured responses for WIPP excavations [7]. Other studies have observed that the empirical modulus ($E_{ref}/12.5$) captured stress relaxation observed in laboratory tests more accurately than the reference modulus (E_{ref}) [8]. Consequently, this empirical adjustment appears to model stress redistribution around openings in rock salt better than the reference modulus when only a secondary creep model is used.

To integrate the constitutive model with time dependent material response, ABAQUS uses an explicit scheme with automatic time step selection in which the time step is calculated to permit a maximum allowable creep strain within a step. In the present calculations, the maximum allowable creep strain was set to 2×10^{-5} . If the maximum creep in a given step exceeds this

value, ABAQUS “steps back” and uses a smaller time step. At earlier times, when the creep rates are high, this solution process results in small time steps (on the order of 1 sec). However, as the calculation progresses, the time step increases to approximately 100 days.

3 ANALYSIS RESULTS

The calculations performed for the four different cavern depths exhibited very similar characteristics. The results for the 3000 ft-deep cavern are presented to illustrate these characteristics since it exhibited the largest deformations. Figure 4 shows the surface subsidence profiles for the 3000 ft-deep cavern. The axis of symmetry is at $x=0$ while the far-field is at $x=375$ ft. The legend on the right corresponds sequentially with the plotted curves from top to bottom. The surface subsidence exhibited in the calculations is uniform across the surface. This implies that for an infinite array of caverns of 750 ft-spacing, the surface subsidence would not result in a patterned array of hills and valleys as was originally expected, but rather the subsidence would be uniform over the entire field.

Figure 5 shows the deformed shape of the 3000 ft-deep cavern at the end of the 30 year simulation. The majority of the deformation occurs at the bottom of the cavern. Figure 6 shows the distribution of the volume loss at time $t=30$ years. The plot is normalized with respect to the total storage loss at $t=30$ years. Fifty percent of the storage loss occurs at the bottom 25 percent of the cavern. Qualitatively, these solutions compare well with independent calculations for a similar cavern design [9].

In the following sections, the effects of cavern depth on storage loss and surface subsidence are investigated. The results are shown from $t = 2$ years to $t = 30$ years since SPR caverns are not typically filled with oil until two or three years after leaching begins. Furthermore, during

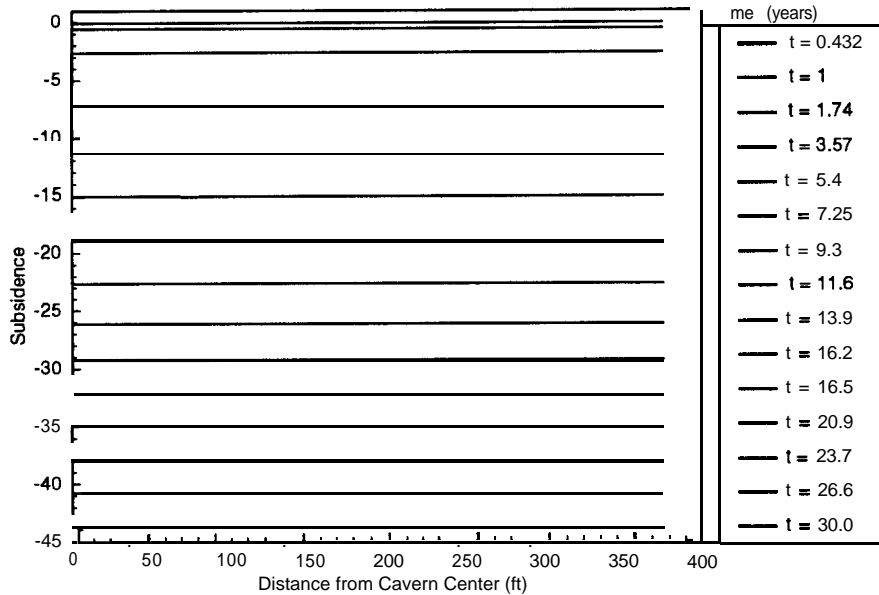


Figure 4. Surface subsidence as a function of time for the 3000 ft-deep cavern.

the first year of the simulations, the pressure history applied to the inside of the cavern is an approximation designed to reduce the high initial creep rates resulting from instantaneous cavern formation (see Section Figure 2.3). This is not a simulation of the complex leaching process but merely an approximation which has been demonstrated to yield better results than instantaneous cavern formation [10]. Thus, the storage loss and subsidence predictions during the first two years are not as significant as the response thereafter.

3.1 Storage Loss

The cavern volume, storage loss, and subsidence volume are plotted as a function of time in Figure 7 through Figure 10 for each of the four cavern depths studied. The curves are normalized with respect to the initial cavern volume (11.2 MMbbl). The plots show that as the cavern depth is increased, the storage loss and subsidence volume increase. Figure 11 shows the percent of storage loss for all four depths as a function of time. Figure 12 shows the percent storage loss at $t = 30$ years as a function of cavern depth. Again these plots show that as the cavern depth is increased the percentage of storage loss increases. There are several reasons for this behavior. First, at greater depths the difference between the lithostatic stress state and the oil pressure is greater. Thus, the effective stresses near the cavern are greater. Based on Equation 3 the resulting creep strain rate will be higher. Second, at greater cavern depths cavern temperatures are higher which, based on Equation 3, results in higher creep strain rates. For exam-

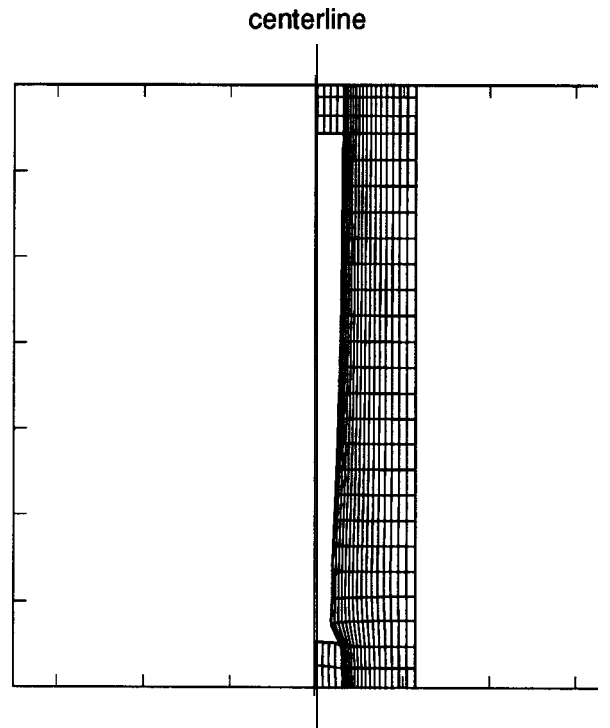


Figure 5. Deformed cavern shape of the 3000 ft-deep cavern at $t=30$ years.

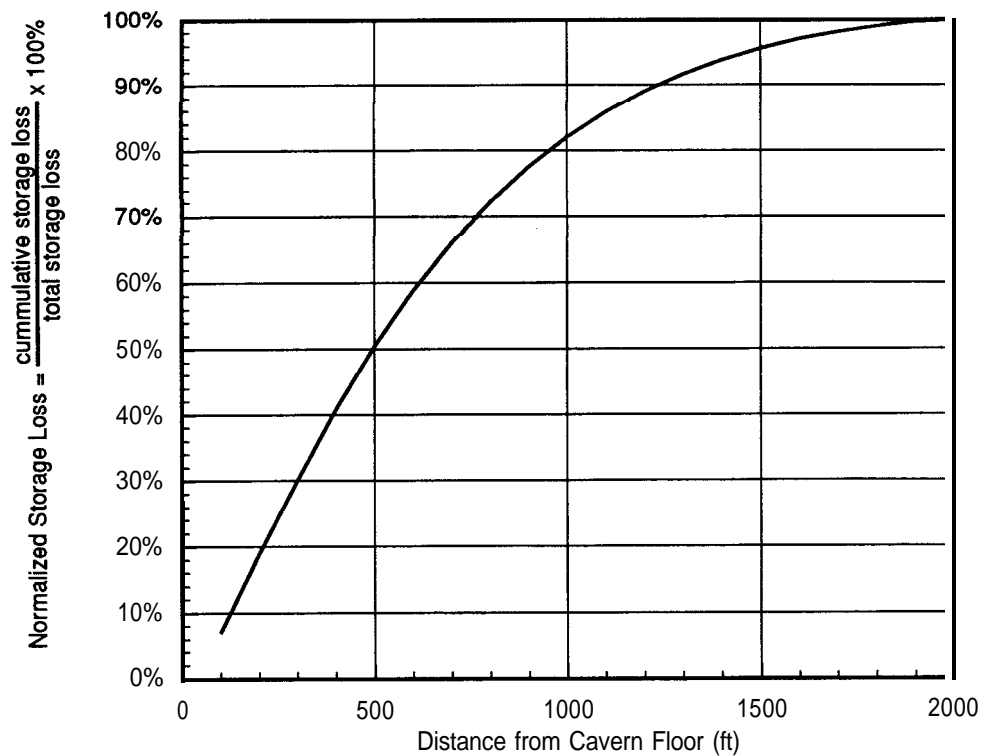


Figure 6. Accumulated storage loss distribution for the 3000 ft-deep cavern as a function of distance measured from the cavern floor to the ceiling. The accumulated storage loss is normalized with respect to total storage loss.

ple, a 3.6° F temperature increase from 80° F will result in a 14 percent increase in creep strain rate. Finally, subsidence and storage loss are affected by the amount of salt above the cavern roof. At lesser depths there is less salt above the room which can creep.

A plot of the storage loss rate as a function of time is shown in Figure 13. The curves show that the storage loss rate increases significantly at greater cavern depths. Again, this is due to the higher creep strain rates around the cavern for the reasons stated above.

3.2 Surface Subsidence

In addition to storage loss, the SPR program is concerned with the effects of parametric changes on surface subsidence. Surface subsidence is plotted in Figure 14 as a function of time for the four cavern depths. The plots show that at greater depths the magnitude of surface subsidence increases. At lesser cavern depths, the subsidence appears to vary more linearly with respect to time. This is due to the fact that the storage loss rate (Figure 13) for caverns at lesser depths approaches a constant rate with respect to time. Figure 15 shows the surface subsidence magnitude at $t=30$ years as a function of cavern depth. Note that the curve shape is very similar to that in Figure 12.

Figure 16 shows the subsidence rate as a function of time for the four cavern depths. As expected, the subsidence rate exhibits a strong dependence on cavern depth. Especially during

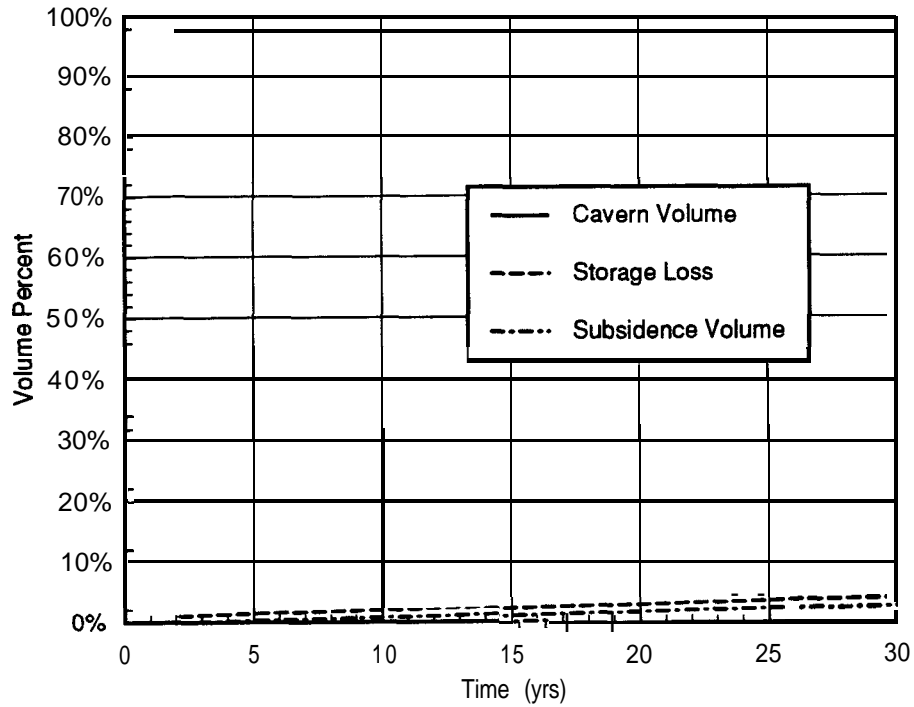


Figure 7. Cavern volume, storage loss and subsidence volume as a function of time for a 1500 ft-deep cavern.

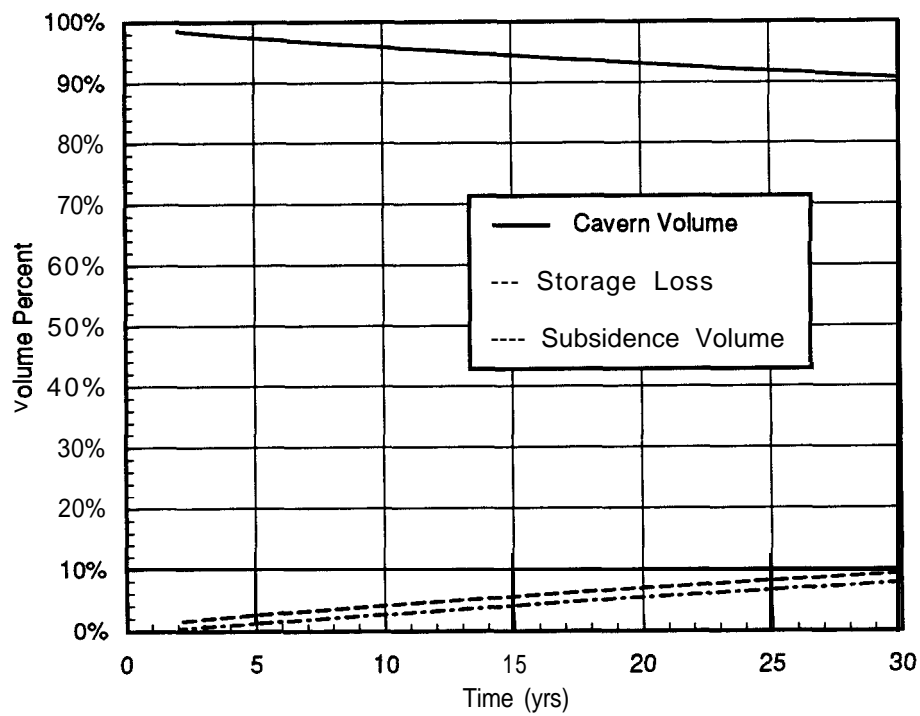


Figure 8. Cavern volume, storage loss and subsidence volume as a function of time for a 2000 ft-deep cavern.

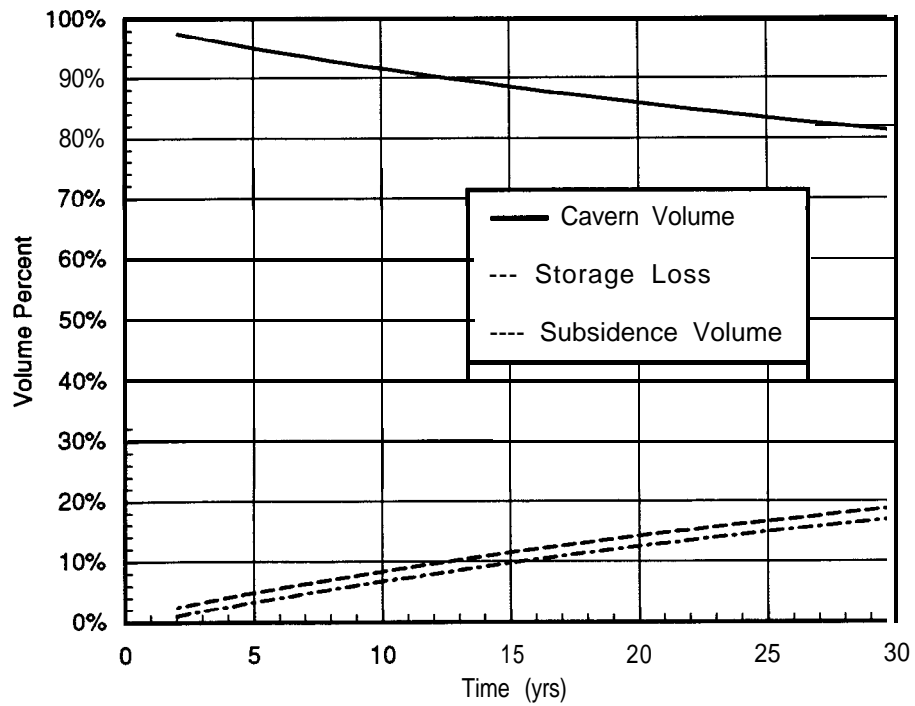


Figure 9. Cavern volume, storage loss and subsidence volume as a function of time for a 2500 ft-deep cavern.

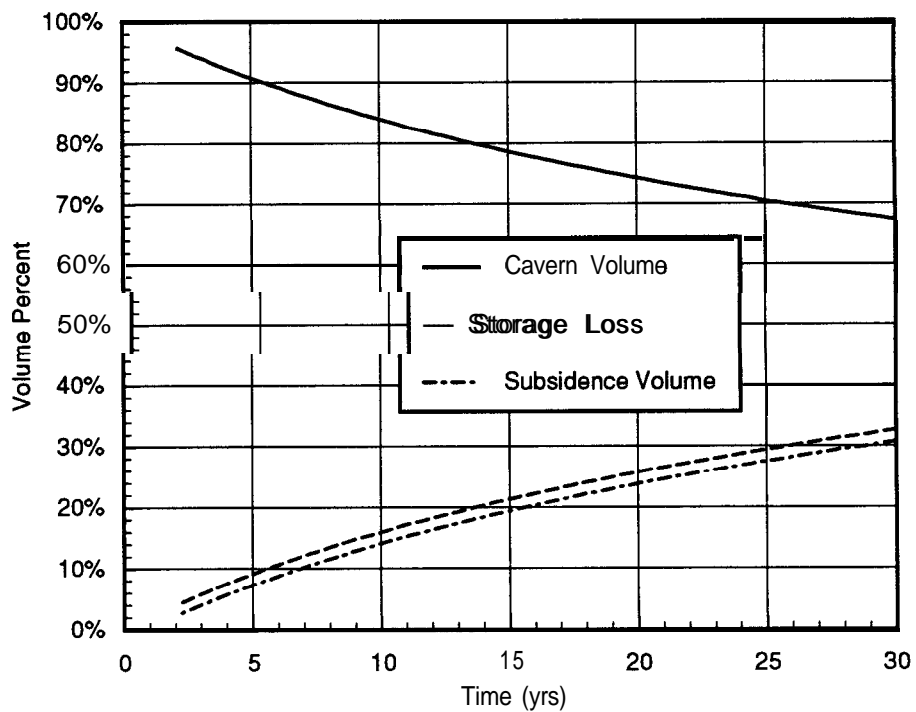


Figure 10. Cavern volume, storage loss and subsidence volume as a function of time for a 3000 ft-deep cavern.

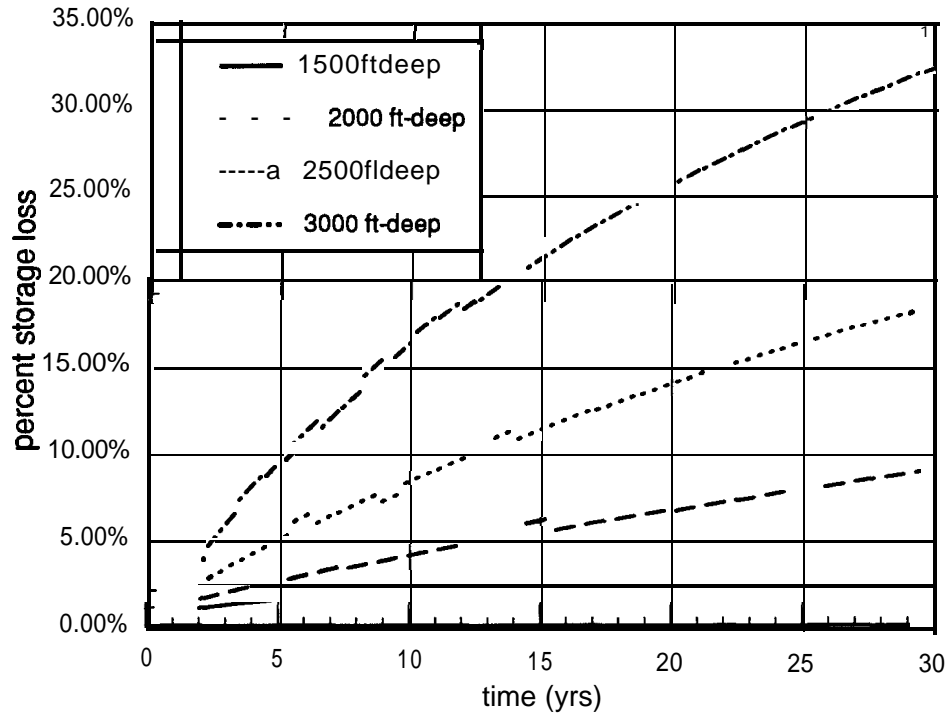


Figure 11. Percent storage loss as a function of time for cavern depths of 1500, 2000, 2500, and 3000 ft.

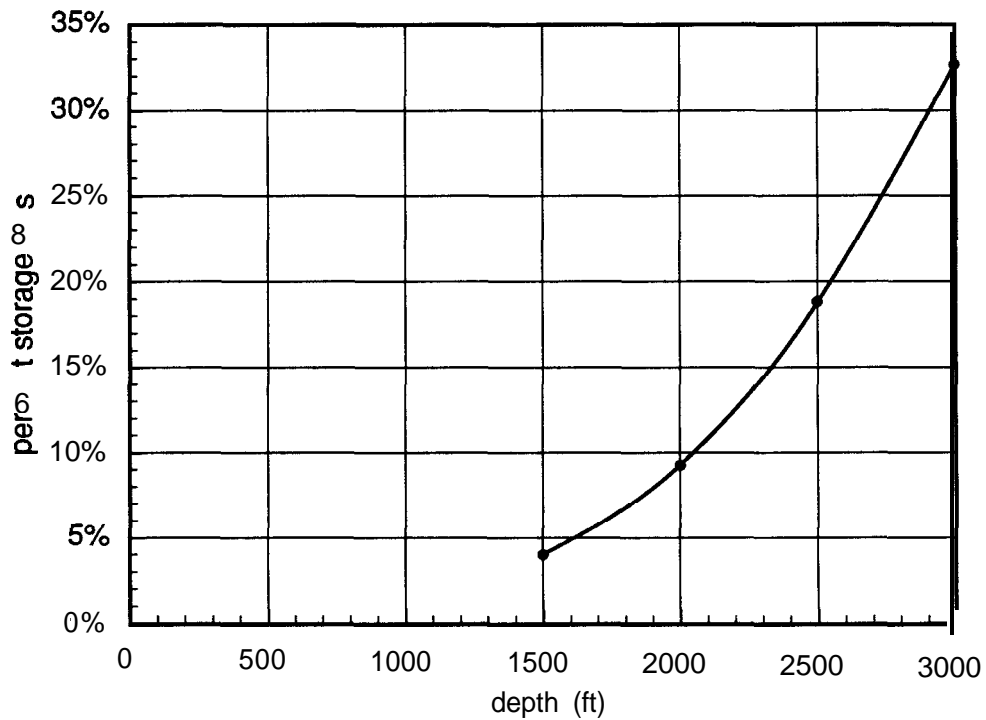


Figure 12. Percent storage loss at 30 years as a function of cavern depth.

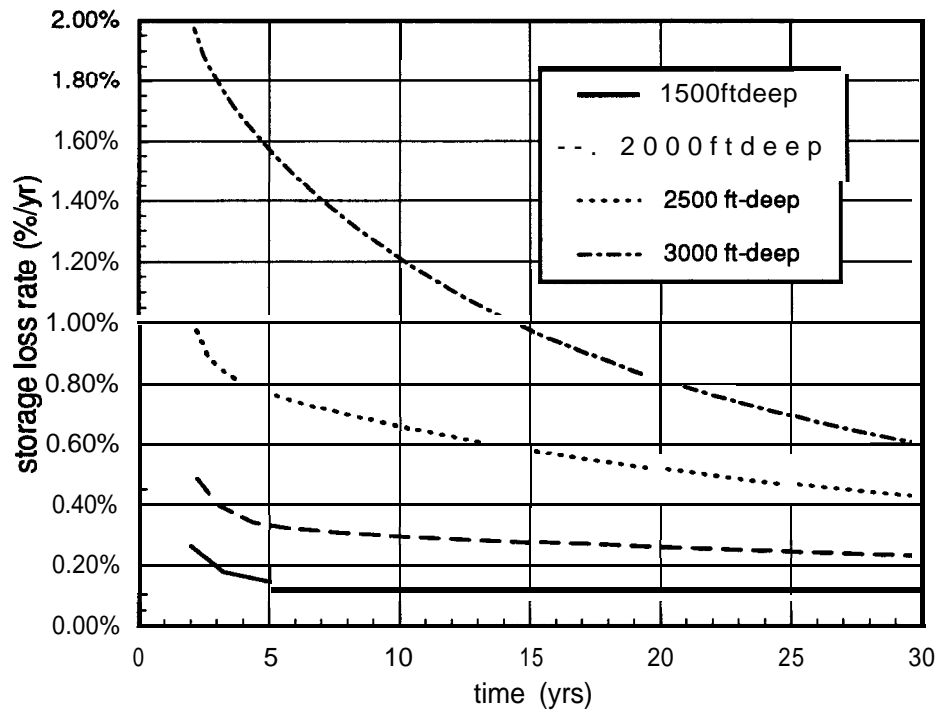


Figure 13. Storage loss rate as a function of time for cavern depths of 1500, 2000, 2500, and 3000 ft.

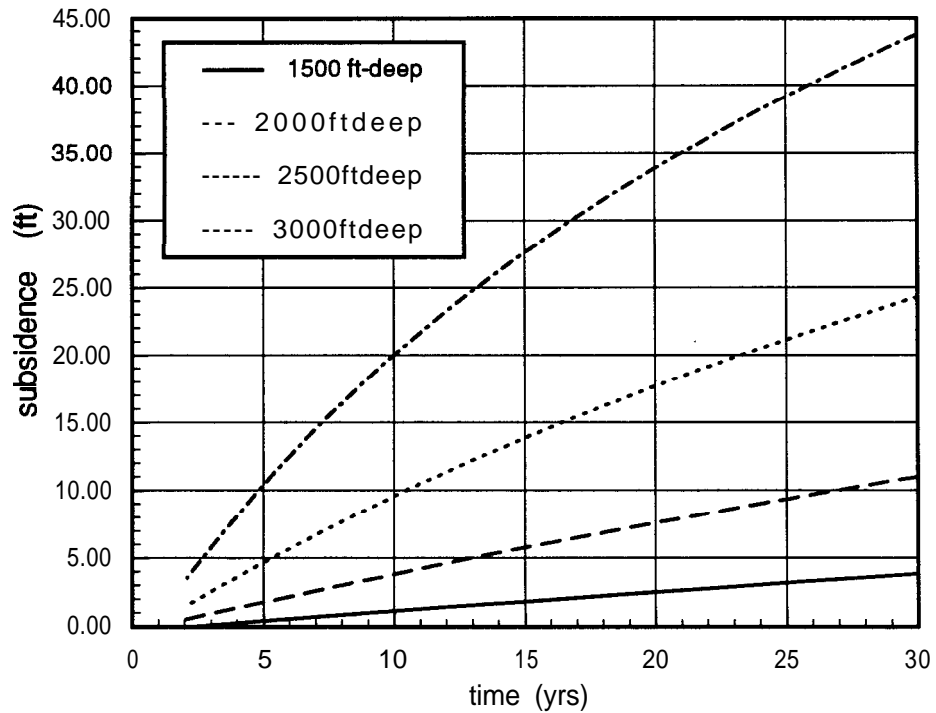


Figure 14. Surface subsidence as a function of time.

the early life of the cavern ($t < 5$ years). This is because subsidence rate is influenced by storage loss rate.

The amount of storage loss which is manifested as surface subsidence is another parameter of interest to the SPR program. It is desirable to minimize surface **subsidence** since it can result in damage to surface structures. Figure 17 shows this volume percentage as a function of time for the four cavern depths. The plots show that the percentage of volume manifested as surface subsidence increases with cavern depth. This seems counter-intuitive, as one would expect that a deeper cavern of similar volume would exhibit **smaller** surface disturbances. However, surface subsidence is actually a direct function of storage loss. For example, the 1500 ft-deep cavern exhibits approximately 4 percent storage loss at thirty years (see Figure 11). The same amount of storage loss is exhibited by the 3000 ft-deep cavern at approximately two years. Comparing these two points in Figure 17 shows that the same volume percentage manifested as surface subsidence is exhibited by the 3000 ft-deep cavern at $t=2$ years as the 1500 ft-deep cavern at $t=30$ years. To better illustrate this relationship, Figure 18 shows a plot of surface subsidence as a function of storage loss. Both axes are normalized with respect to the original cavern volume. The curves coincide with one another in a nearly-linear relationship between surface subsidence and storage loss. The relationship is not one-to-one since a small percentage of storage loss is not manifested as surface subsidence. Based on these observations, it can be concluded that a region of finite extent exists, both above and below the cavern, which is influenced by the presence of a cavern in an infinite array. The creep strains occur only in that region. The column of material above that region, including the **caprock** and overburden, follows along in rigid body displacement.

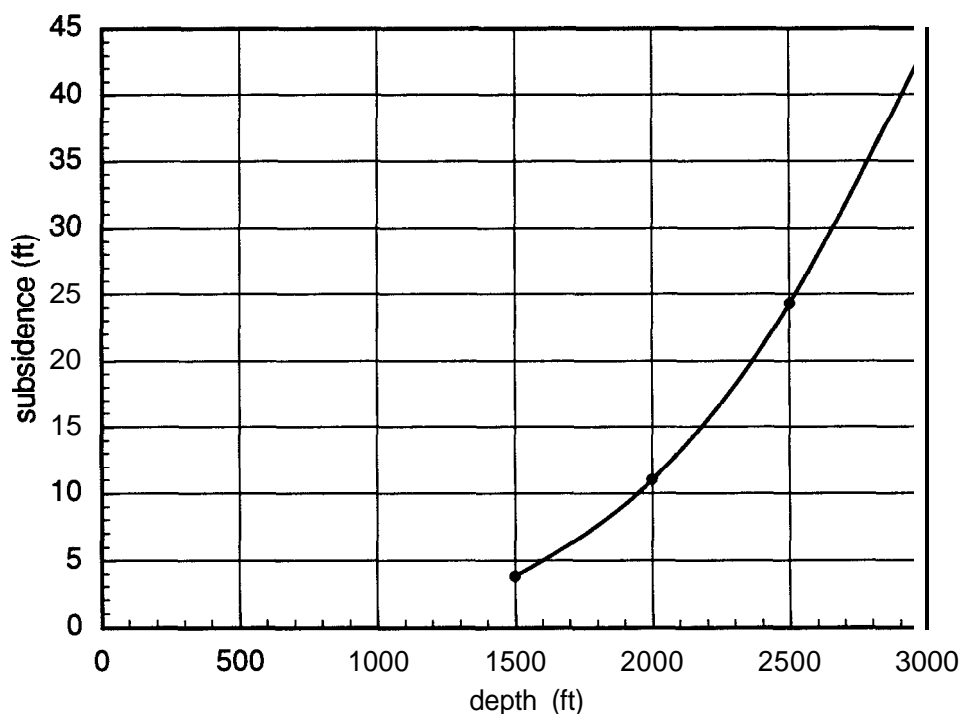


Figure 15. Surface subsidence at $t=30$ years as a function of cavern depth.

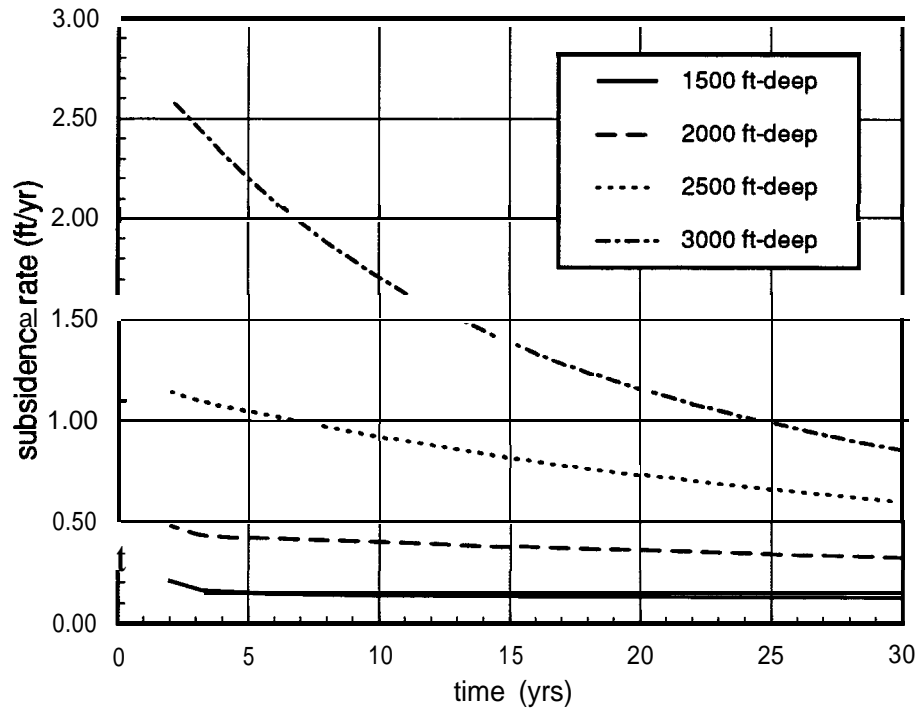


Figure 16. Subsidence rate as a function of time for cavern depths of 1500, 2000, 2500, and 3000 ft.

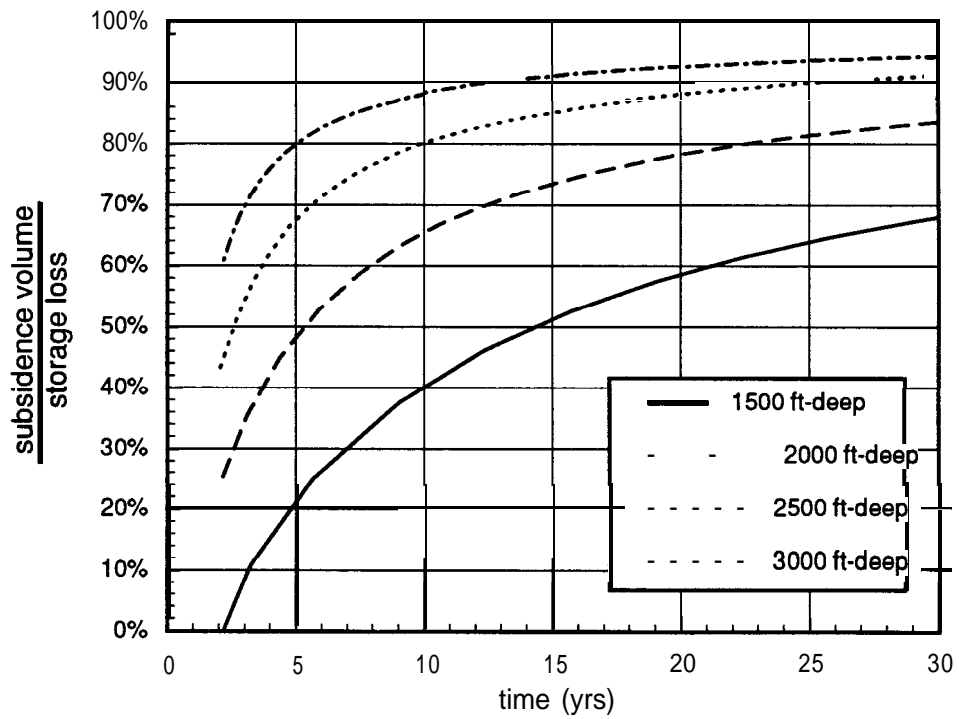


Figure 17. Fraction of storage loss converted to subsidence as a function of time.

Based on observation of Figure 7 through Figure 10, it appears that the difference between storage loss and subsidence volume remains constant with respect to time. The difference between the storage loss and the subsidence volume is plotted in Figure 19 for the four cavern depths. The volume difference is normalized with respect to the initial cavern volume. This plot shows that for a given cavern depth, the volume difference is established early in the cavern life and stays nearly constant thereafter. Furthermore, the difference is depth dependent. Greater cavern depths result in a larger difference between the storage loss and subsidence volume. However, this difference is small ($>0.25\%$) compared to the initial volume of the cavern.

A difference between the storage loss and the subsidence volume could occur due to the numerics of the problem. If a mismatch exists between the applied initial stresses and equilibrium, an instantaneous volume difference would occur as the solution found equilibrium. However, the volume difference observed in Figure 19 develops slowly over the first year, indicating that it is not developed from a numerical imbalance. Since the constitutive model used for salt does not consider volumetric creep, the volume difference cannot be in creep strains. Thus, the volume difference must be due to an elastic volumetric strain above the cavern.

3.3 Comparison of Analysis Results to Field Measurements

The finite element calculations were verified by comparing results from the base case of a 2500 ft-deep cavern to field measurements taken from West Hackberry Cavern 115. This cavern was chosen for comparison because it has similar storage capacity, dimensions, and loca-

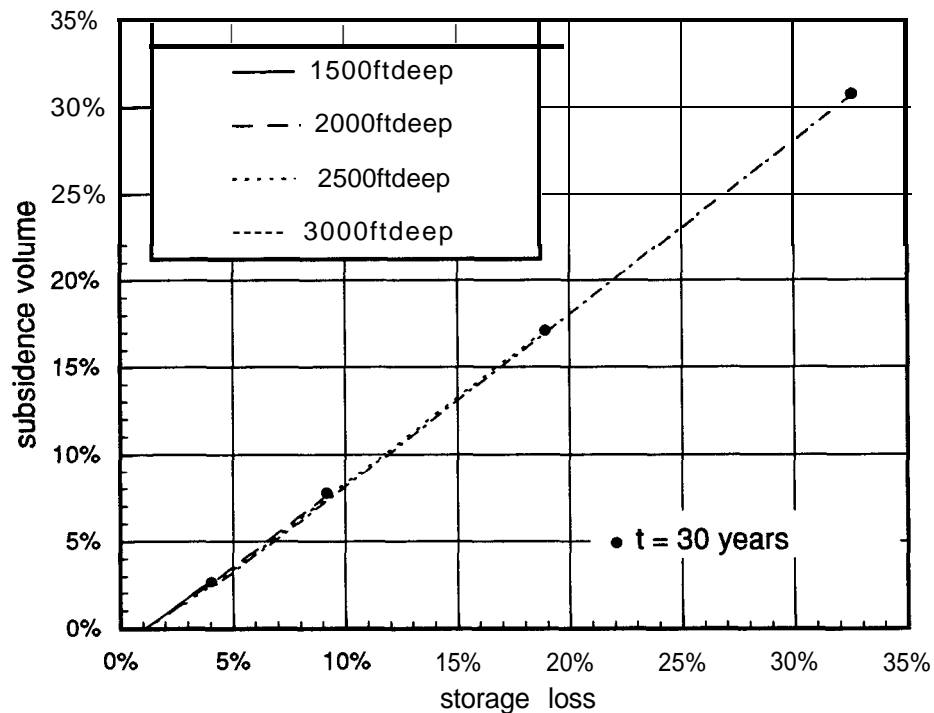


Figure 18. Surface subsidence as a function of storage loss. Both variables are normalized with respect to the original cavern volume.

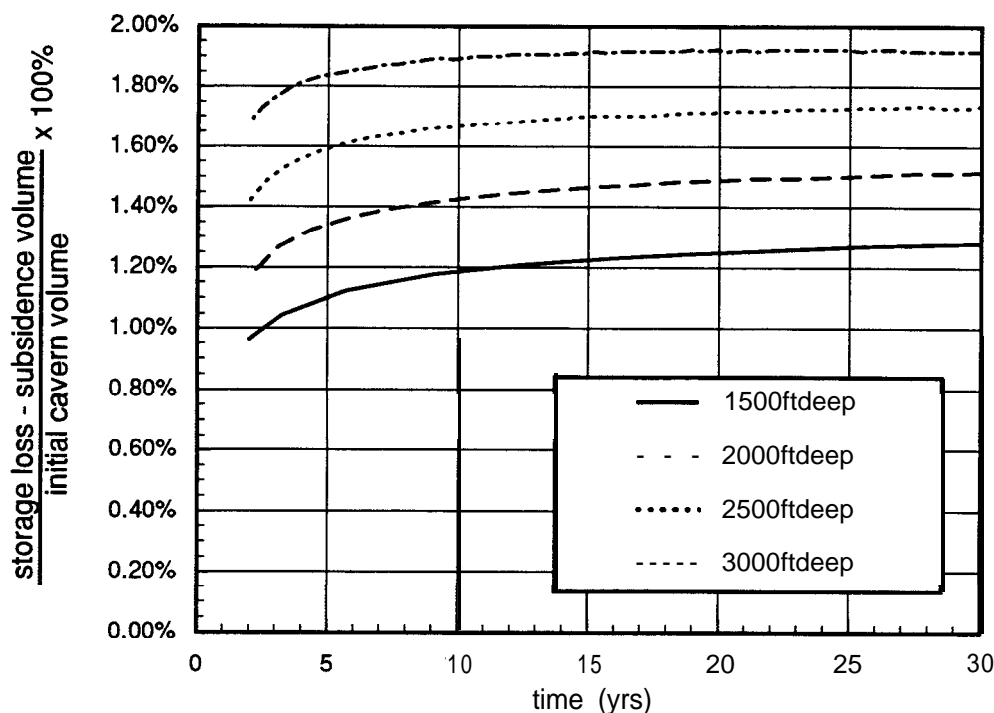


Figure 19. Difference between storage loss and subsidence volume for cavern depths of 1500, 2000, 2500, and 3000 ft.

tion as the 2500 ft-deep model. Cavern 115 is centrally located at approximately 750 ft from six neighboring caverns, closely approximating the infinite array assumption used for the model. However, because it is actually not part of an infinite array, the extent of the subsidence and closure should be less than the analysis results. It should be emphasized that the model was not intended to simulate Cavern 115. The purpose of the comparison is merely to qualitatively evaluate the analyses by demonstrating that the subsidence and storage loss are of the same order-of-magnitude as the field data since the geometries are similar.

The measured subsidence at West Hackberry Cavern 115 is given in Table 2. The measurements were made while the cavern was being leached and filled. The fluctuation of the subsidence rate is due to the fact that the cavern was not filled with oil until the September 16 measurement. At nearly five years, the total measured subsidence was 1.43 ft. The predicted subsidence for the 2500 ft-deep cavern was 4.9 ft, a factor of 3.4 greater. The predicted subsidence rate for the 2500 ft-deep cavern is approximately 1 ft/yr, approximately four times higher than the field measurements.

Another metric of cavern performance is well pressure. As the cavern volume decreases, the well pressure at the surface increases. Pressurization data have been measured for West Hackberry Cavern 115 and are given in Table 3 for a one-year time interval. The cavern is approximately 9 years old at the start of the data. Assuming the oil temperature does not change, cavern pressure can be related to volumetric losses by the compressibility of oil ($5.67 \times 10^{-6} \text{ psi}^{-1}$ at API=37.5, P=2265 psi, and T=125 °F). Based on the instantaneous cavern volume, the

predicted pressurization rate from the analysis is plotted in Figure 20. The predicted pressurization rate for a 9 year-old cavern is 3.5 psi/day. The prediction is higher than the field measurements (approximately 2 psi/day); however, again the model assumes the cavern is located in an infinite array of caverns.

Although the predictions are at least a factor of two larger than the field measurements, these comparisons have demonstrated that the analysis results are of the same order-of-magnitude as the data. These calculations were not performed to model Cavern 115; therefore, model details such as cavern geometry may not be accurately representative of this cavern and could affect the results.

Table 2: Measured Subsidence at West Hackberry Cavern 115

Date	Elevation Above Sea Level (ft)	Accumulated Subsidence (ft)	Subsidence Rate (ft/yr)
1/83	9.15		
8/83	9.07	0.08	.137
2/84	8.87	0.28	.400
3/85	8.43	0.72	.406
9/86	8.03	1.12	.267
12/87	7.72	1.43	.248

Table 3: Measured Pressurization Data for West Hackberry Cavern 115

Date	Start Pressure (psi)	Pressure Change (psi)	Duration Cycle (days)	Pressurization Rate (psi/day)
11/2/89	930	80	39	2.1
1/25/90	920	100	55	1.8
3/22/90	930	85	43	2.0
5/4/90	910	60	27	2.2
5/31/90	910	100	56	1.8
7/27/90	930	80	49	1.6
10/2/90	910	85	50	1.7

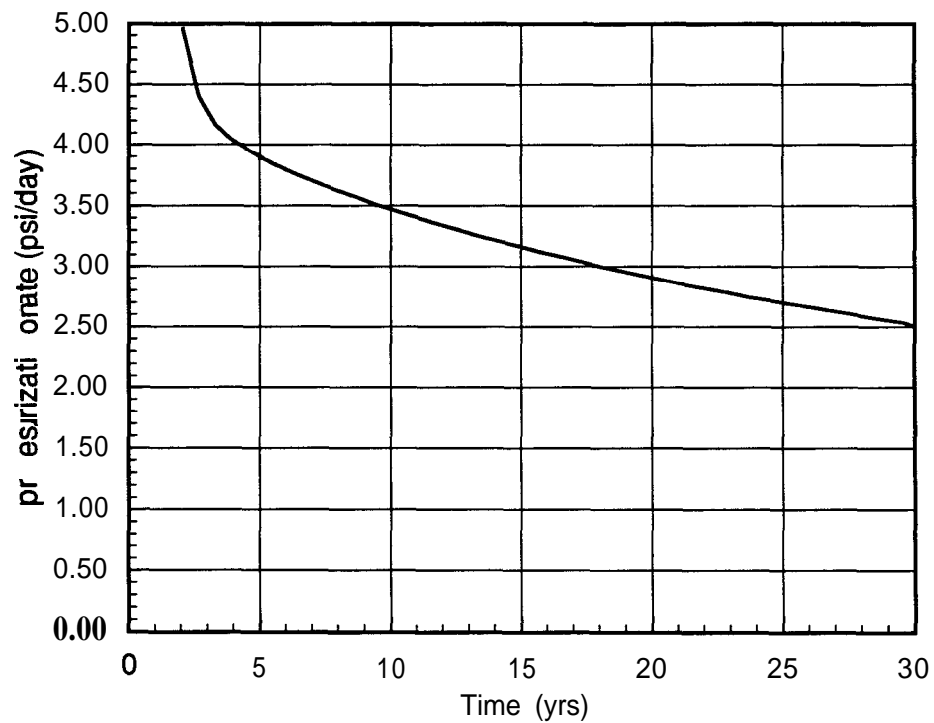


Figure 20. Pressurization rate for the 2500 ft-deep cavern.

4 CONCLUSIONS

In the preceding calculations, the effect of cavern depth on storage loss and surface subsidence was investigated. The results indicate that in an infinite array of caverns both subsidence and storage loss are strongly influenced by cavern depth. The results of the base case (2500 ft-deep cavern) calculations compared reasonably well with independently performed calculations of a similar cavern design [9]. Based on these calculations, the following conclusions can be made:

1. Storage loss increases with increasing depth because at lower depths the difference between the local lithostatic stress and the oil pressure is greater. Thus, the effective stresses are greater, resulting in higher creep rates. Furthermore, at greater depths the cavern temperatures are higher and produce higher creep rates.
2. Surface subsidence is directly related to the amount of storage loss. Deeper caverns exhibit more subsidence because the caverns exhibit more storage loss. However, for a given amount of storage loss, nearly the same magnitude of surface subsidence was exhibited, independent of cavern depth.
3. The difference between the storage loss and surface subsidence exhibits a dependence on cavern depth. For a 500 ft increase in depth, this volume difference increased by an amount equal to 0.25 percent of the initial cavern volume. This volume difference is developed in the early life of the cavern and approaches a constant steady state value for the remainder of the cavern life. The volume difference is due to elastic volumetric strains developed above the cavern.
4. Comparison of analysis predictions for the 2500 ft-deep cavern with field data from West Hackberry Cavern 115 show order-of-magnitude agreement. Subsidence, subsidence rate, and pressurization predictions were larger than the field measurements; however, this was expected since the analysis assumes the cavern is located in an infinite array of caverns.

5 REFERENCES

- 1 Hibbitt, Karlson, and Sorensen, **ABAQUS User's Manual, Version 4.8**, 1989.
- 2 G. D. Sjaardema, **Aprepro: An Algebraic Preprocessor for Input Files**, memo to Distribution, Sandia National Laboratories, Albuquerque, NM, May 18, 1990.
- 3 R. S. Carmicheal, **Handbook of Physical Properties of Rocks**, Vol. 2 of 3.
- 4 R. D. Krieg, **Reference Stratigraphy and Rock Properties for the Waste Isolation Pilot Plant (WIPP) Project**, SAND83-1908, Sandia National Laboratories, Albuquerque, NM, January 1984.
- 5 W. Herrmann and H. S. Lauson, **Analysis of Creep Data for Various Natural Rock Salts**, SAND81-2567, Sandia National Laboratories, Albuquerque, NM, December 1981.
- 6 W. Hermann and H. S. Lauson, **Review and Comparison of Transient Creep Laws Used for Natural Rock Salt**, SAND81-0738, Sandia National Laboratories, Albuquerque, NM, April 1981.
- 7 H. S. Morgan and R. D. Krieg, **A Comparison of Unified Creep Plasticity and Conventional Creep Models for Rock Salt Based on Predictions of Creep Behavior Measured in Several In-Situ and Benchscale Experiments**, SAND87-1867, Albuquerque, NM, April, 1988.
- 8 H. S. Morgan and R. D. Krieg, **Investigation of an Empirical Creep Law for Rock Salt that Uses Reduced Elastic Moduli**, Rock Mechanics Contributions and Challenges: Proceedings of the 31st U.S. Symposium, A.A. Balkema Publishers, Brookfield, VT, 1990, pp. 965-972.
- 9 B. L. Ehgartner, **Effects of Cavern Spacing and Pressure on Subsidence and Storage Losses for the US SPR**, memo to Distribution, SAND91-2575, Sandia National Laboratories, Albuquerque, NM, February 1992.
- 10 D. S. Preece and J. T. Folley, **Long-Term Performance Predictions for Strategic Petroleum Reserve (SPR) Salt Caverns**, SAND83-2343, Sandia National Laboratories, Albuquerque, NM, November 1984.

Distribution

US DOE SPR PMO (5)
900 Commerce Road East
New Orleans, LA 70123
Attn: D. W. Whittington, PR-622
R. Myers, PR-622
L. Rousseau, FE-443
TDCS (2)

US DOE SPR (2)
1000 Independence Avenue SW
Washington, DC 20585
Attn: D. Johnson
D. Smith

Boeing Petroleum Services (3)
850 S. Clearview Parkway
New Orleans, LA 70123
Attn: K. Wynn
T. Eyerman
K. Mills

Boeing Petroleum Services (1)
1450 Black Lake Road
Hackberry, LA 70645
Attn: J. Perry

Tejas Power Corporation (1)
148 11 St. Mary's Lane
Suite 200
Houston, TX 77079
Attn: Greg Graves

Sandia Internal:

1425 J. H. Biffle
1430 J. R. Asay
1434 D. R. Martinez
1510 J. C. Cummings
1550 C. W. Peterson
1561 H. S. Morgan
1561 E. L. Hoffman (6)
1561 C. M. Stone
1562 R. K. Thomas, Acting
6200 B. W. Marshall
6250 P. J. Hommert
6252 J. C. Dunn
6253 D. A. Northrop
6253 D. S. Preece
6257 J. K. Linn (10)
6257 S. J. Bauer
6257 B. L. Ehgartner
6257 T. E. Hinkebein
6257 P. S. Kuhlman
6257 R. V. Matalucci
6257 J. T. Neal
6257 J. L. Todd
6257 S. T. Wallace
6258 M. W. Scott
6346 D. E. Munson
8523-2 Central Technical Files
3141 S. A. Landenberger (5)
3145 Document Processing for DOE/
OSTI (8)
3151 G. C. Claycomb (3)